IOP Publishing Phys. Med. Biol. 69 (2024) 115015 https://doi.org/10.1088/1361-6560/ad42fd

Physics in Medicine & Biology

IPEM Institute of Physics and Engineering in Medicine

OPEN ACCESS

RECEIVED
13 February 2024

REVISED
27 March 2024

ACCEPTED FOR PUBLICATION
24 April 2024

PUBLISHED
20 May 2024

PAPER

Spread-out Bragg peak measurements using a compact quality assurance range calorimeter at the Clatterbridge cancer centre

Saad Shaikh[1], Sonia Escribano-Rodriguez[1], Raffaella Radogna[2], Laurent Kelleter[3], Connor Godden[1], Matthew Warren[1], Derek Attree[1], Ruben Saakyan[1], Linda Mortimer[4], Peter Corlett[4], Alison Warry[5], Andrew Gosling[5], Colin Baker[5], Andrew Poynter[5], Andrzej Kacperek[6] and Simon Jolly[1]

[1] Department of Physics and Astronomy, University College London, London, United Kingdom
[2] Department of Physics, University of Bari, Bari, Italy
[3] Division of Medical Physics in Radiation Oncology, German Cancer Research Centre (DKFZ), Heidelberg, Germany
[4] Clatterbridge Cancer Centre NHS Foundation Trust, Wirral, United Kingdom
[5] Proton Beam Therapy Physics, University College London Hospital NHS Foundation Trust, London, United Kingdom
[6] Department of Medical Physics and Biomedical Engineering, University College London, London, United Kingdom

E-mail: saad.shaikh@ucl.ac.uk

Keywords: proton therapy, plastic scintillator, spread out Bragg peak, quality assurance

Abstract

Objective. The superior dose conformity provided by proton therapy relative to conventional x-ray radiotherapy necessitates more rigorous quality assurance (QA) procedures to ensure optimal patient safety. Practically however, time-constraints prevent comprehensive measurements to be made of the proton range in water: a key parameter in ensuring accurate treatment delivery. *Approach.* A novel scintillator-based device for fast, accurate water-equivalent proton range QA measurements for ocular proton therapy is presented. Experiments were conducted using a compact detector prototype, the quality assurance range calorimeter (QuARC), at the Clatterbridge cancer centre (CCC) in Wirral, UK for the measurement of pristine and spread-out Bragg peaks (SOBPs). The QuARC uses a series of 14 optically-isolated 100 × 100 × 2.85 mm polystyrene scintillator sheets, read out by a series of photodiodes. The detector system is housed in a custom 3D-printed enclosure mounted directly to the nozzle and a numerical model was used to fit measured depth-light curves and correct for scintillator light quenching. *Main results.* Measurements of the pristine 60 MeV proton Bragg curve found the QuARC able to measure proton ranges accurate to 0.2 mm and reduced QA measurement times from several minutes down to a few seconds. A new framework of the quenching model was deployed to successfully fit depth-light curves of SOBPs with similar range accuracy. *Significance.* The speed, range accuracy and simplicity of the QuARC make the device a promising candidate for ocular proton range QA. Further work to investigate the performance of SOBP fitting at higher energies/greater depths is warranted.

1. Introduction

Proton beam therapy (PBT) has seen a rapid increase in the number of patients treated worldwide over the last few decades, with around 100 operational centres active today (Particle Therapy Co-operative Group 2023). Compared to conventional x-ray radiotherapy, PBT provides superior dose conformity due to the energy loss characteristics of protons, resulting in a lower proximal dose that rises to a pronounced maximum—the Bragg Peak—with minimal distal dose beyond this when compared to x-rays (Paganetti 2012). This resulting finite range of protons in matter, whilst enabling a superior dose conformity, makes PBT more sensitive to both patient setup and planning errors (such as incorrect tumour demarcation, uncertainties in patient tissue stopping power etc (Lomax 2008b, 2008a)) and position and range inaccuracies in the delivered proton beam. In order to constrain the delivered beam characteristics to within the necessary clinical tolerances, a series of quality assurance (QA) procedures are carried out at regular intervals to ensure safe operation of the proton beam

facility (Ding *et al* 2021). Guidelines recommend checks on the absolute dose, size, lateral position and range-in-water of the delivered proton beam (Arjomandy *et al* 2019). However, due to a lack of an internationally agreed standard, these guidelines emphasise that individual facility experience should inform best practice. Henceforth, 'Quality Assurance' and 'QA' refers to these beam-specific QA procedures to ensure the proton beam delivers dose to the correct clinically-prescribed location.

Daily QA procedures are carried out before treatment begins to ensure the proton beam is safe for clinical delivery and that there is no significant variation in proton beam parameters from the previous day's treatment. These are by necessity faster and less comprehensive than weekly, monthly or yearly checks meaning that compromises must be made to ensure treatment time is not impacted by excessively laborious daily QA procedures. Of the beam QA measurements, proton range-in-water is the least often measured directly (Ding *et al* 2021). Whilst it is possible to measure proton beam size and position directly with scintillator screen-based detectors and commercial ionisation chambers exist for rapid measurements of absolute dose (Bäumer *et al* 2015, Ion Beam Applications 2023c), proton range-in-water is normally inferred from beam size or dose deposition measurements after passing through absorbers of precisely calibrated thickness. The most commonly used commercially available example of which is the IBA Lynx-Sphinx (Russo *et al* 2017, Placidi *et al* 2018, Rana *et al* 2019, Su *et al* 2020, Ion Beam Applications 2023b, 2023d). This makes full measurements of not just the Bragg curve but also the proton range for a given energy impractical for daily QA: time limitations mean the 'range' is normally sampled at ∼3 locations along the Bragg curve for a few predefined energies. Primarily due to detector setup complexity, full Bragg curve measurements for the complete range of energies deliverable from a clinical PBT nozzle are reserved for less frequent checks with less immediate time pressure on patient treatment: these utilise ionisation chamber-based systems capable of making depth dose curve measurements with millimetre or sub-millimetre accuracy, such as the PTW Peakfinder (Physikalisch-Technische Werkstaetten 2023) or the IBA Giraffe and Zebra systems (Ion Beam Applications 2023a, 2023e). Whilst providing full depth dose curve measurements in seconds, rather than the minutes for a moving-detector system like the Peakfinder, multi-layer ionisation chamber (MLIC)-based systems such as the IBA Giraffe/Zebra sacrifice depth resolution and compromise on water-equivalency through the use of aluminium beam degrader plates. In addition, ionisation chambers exhibit a dose-rate dependence at ultra-high dose rates ('FLASH') (McManus *et al* 2020), which make QA for FLASH treatments challenging (Jolly *et al* 2020).

2. Ocular proton beam therapy at the Clatterbridge cancer centre

Established as the first hospital-based PBT centre, the Clatterbridge cancer centre (CCC) has been treating ocular tumours (primarily uveal melanomas) since 1989 (Kacperek 2009). The Scanditronix MC-60 PF isochronous cyclotron produces 62.5 MeV protons bunched at 25.78 MHz that are then transported through a passive double scattering (DS) beam delivery system, resulting in a uniform circular 60 MeV proton beam that is 33.5 mm in diameter at the nozzle exit (Bonnett *et al* 1993, Yap *et al* 2020). The required lateral beam area is provided not by scanning the beam across the tumour volume but with a patient-specific brass collimator—machined to the full lateral extent of the specific tumour—that collimates the transverse profile of the beam to match the shape of the lateral target area (Kacperek 2009). The depth-dose distribution is then produced with a stepped patient-specific range modulator wheel, machined from PMMA plastic and inserted approximately 1 m upstream of the nozzle, which rotates at ∼400 rpm and produces the spread-out Bragg peak (SOBP) necessary for treatment. A fixed PMMA absorber can then be used to further reduce the entire SOBP range as required to match the depth of the tumour (Kacperek 2009). The measurements needed for beam QA at the CCC differ from the modern pencil beam scanning (PBS) facility in a number of aspects: since there is no beam scanning, spot position and shape measurements are replaced by transverse uniformity and SOBP modulation measurements to ensure that there is no lateral dose delivery variation across the beam. While the DS beamline produces a beam that is approximately monoenergetic at 60 MeV with a corresponding range in eye tissue of 29.2 mm, depth-dose curve measurements are required for each individual patient treatment plan since the range modulator is unique to each patient treatment, necessitating patient-specific QA (PSQA).

Depth-dose curve QA measurements are carried out with a 3×3 mm^2 diode mounted behind a ∼30 cm diameter stepped PMMA wheel with 0.15 mm range steps (Kacperek 2009). The wheel is rotated with a stepper motor that allows the depth-dose curve to be sampled in 0.15 mm water-equivalent steps. This assembly mounts to the support structure below the nozzle, locating the diode directly on the beam axis, thereby reducing the setup time since neither a bespoke support structure or precision alignment is required prior to measurement. However, whilst the measurement is relatively simple compared to a multi-energy PBS nozzle, setup and measurement time mean that daily QA measurements can take up to 30 minutes, with multiple PSQA measurements taking several hours. Since range QA forms an essential part of both daily beam QA and PSQA,

reducing both the setup and measurement time for the range QA measurement has the potential to both reduce the clinical workload and increase the treatment capacity of the single treatment room.

3. The quality assurance range calorimeter (QuARC)

Organic plastic scintillators have been an area of significant research for their applications in dosimetric measurements in PBT due to their low cost, fast response times, and near water-equivalence (Beaulieu and Beddar 2016). However, scintillators are generally avoided for absolute dosimetry and depth-dose measurements due to the scintillator light quenching effect, where the scintillation light output becomes non-linear with increasing linear energy transfer (LET) (Birks 1951). In addition, light degradation from radiation damage limits the lifespan of scintillator-based detectors when compared to systems that utilise ionisation chambers. Current commercial uses of scintillators in PBT have been largely limited to scintillator screens for the measurement of proton field homogeneity, such as the IBA Lynx (Ion Beam Applications 2023b). While the Lynx provides an integrated QA system—when combined with the IBA Sphinx QA phantom (Ion Beam Applications 2023d)—that is becoming more popular for PBS daily QA, direct depth-dose curve measurements are not possible, with depth-dose information only inferred from the relative beam spot intensity on the scintillator screen having passed through an absorber of known thickness. However there have been several research developments over the last decade in large-volume scintillators for the measurement of proton range.

Most recently, a detector utilising a monolithic scintillator block imaged from multiple angles with charge-coupled device cameras has been developed to make measurements of proton depth-light curves and spots for QA and proton radiography purposes (Darne *et al* 2017, 2022). Results with this device have been promising, with range QA measurements shown to be accurate to 0.1mm and the multi-camera setup allowing for precise tracking of beam position in 3D. However, the main drawback of this setup—and indeed any setup that uses a camera to image the scintillator—is the need to correct for optical artefacts in order to recover accurate depth-light curves, which necessitates careful optical calibration of the device (Robertson *et al* 2013). Additionally, the cameras must be placed at a distance (around 80 cm) from the scintillator in order to focus the lens, which significantly increases the overall size of the detector and makes it less practical to implement in the clinic. High-resolution simulations of the LET distribution are also required in order to correct for scintillator light quenching, which are susceptible to misalignment relative to experimental measurements (Robertson *et al* 2012).

An alternative is to segment the scintillator block into a series of optically-isolated sheets and collect the light output from each of these sheets individually. Whilst reducing the longitudinal resolution significantly—from the pixel resolution of the camera to the thickness of each scintillator sheet—and discarding the possibility of recording transverse beam position information, there are several advantages to such a setup:

- Coupling the light readout directly to the scintillator sheets significantly reduces the transverse dimensions of the detector, making the detector smaller and easier to handle and comparable in size to an MLIC.
- Optical artefact correction is no longer needed since the entire light output of each sheet is integrated by the light detector. In particular, parallax errors—whereby the derived range is dependent upon the proximity of the beam to the camera—are no longer an issue.
- The larger amount of light available to each light detector increases the available frame-rate, opening the possibility for spot-by-spot measurements.
- The reduced detector size opens the possibility of mounting the entire detector assembly on the clinical nozzle, simplifying setup and alignment.

A novel range/SOBP QA device based upon this latter principle has been developed that can provide real-time, water-equivalent measurements of proton range to sub-mm precision in a compact, self-contained package that can be mounted onto the proton beam nozzle. This device builds on a proof-of-concept prototype that used a series of painted scintillator sheets coupled to a flat-panel CMOS sensor for measurements of proton range (Kelleter *et al* 2020). This prototype was capable of measuring the proton range accurate to within 0.5 mm with just a single beam delivery, and without the need to correct for optical artefacts or simulate the LET distribution to correct for light quenching. The detector was also found to be suitably radiation hard within the expected operational lifetime of a commercial device. However, the CMOS sensor used for light measurement was found to be highly sensitive and would often saturate with clinical beams. Involved image analysis was also required to extract the light output for each scintillator sheet, which combined with the slow sensor frame-rate made real-time range reconstruction infeasible. Finally, the size of the detector was limited by the size of the sensor itself and was not conducive to the modular design goals for the device.

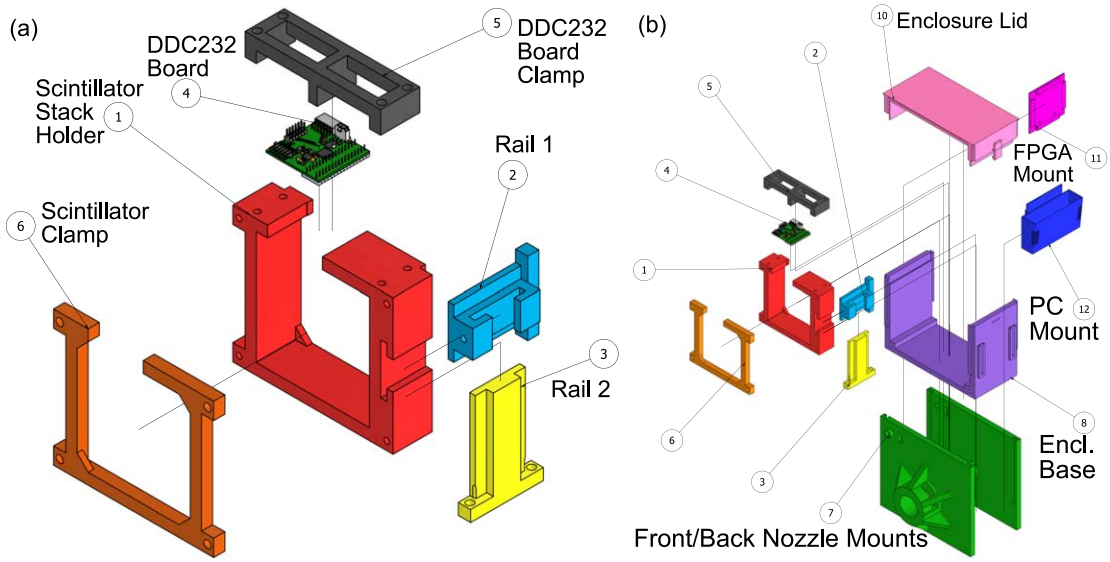

Figure 1. CAD schematics for the (a) 3D-printed scintillator stack holder and (b) detector enclosure, showing attachments for the stack holder and external electronics. DDC232 described in section 4.1.2.

As a result, a completely new detector readout system was developed which considerably increases the ease-of-use, dynamic range and readout speed of the detector. This new system, the QuARC, improves upon the previous design by replacing the flat-panel CMOS sensor with photodiodes individually coupled to each scintillator sheet. The size of the photodiodes matches the thickness of the scintillator sheets, which enables direct measurement of individual sheet light output without the need for any image analysis. The photodiodes are then read out with a fast current-integrating analogue-to-digital converter (ADC) that enables beam measurements in excess of 5 kHz, thereby enabling spot-by-spot measurements for dwell times above 200 μs. In this work, a compact version of the QuARC has been developed for ocular proton therapy at the CCC showcasing this new readout system to perform range QA measurements of both pristine and spread-out Bragg peaks.

4. Materials and methods

4.1. Detector design

4.1.1. Mechanical assembly

The prototype developed in this work uses 14 NUVIATech Instruments NuDET SP32 plastic scintillator sheets of size 100 × 100 × 2.85 mm (NUVIATech Instruments 2019). This polystyrene-based scintillator has peak emission at 425 nm, refractive index of 1.57, density of 1.03 g cm^{-3}, light output 56% of anthracene and decay constant of 2.5 ns. The scintillator sheets are housed in a custom 3D-printed holder made of black Ultimaker tough polylactic acid (PLA) (Ultimaker 2018). The CAD schematic for the stack holder is shown in figure 1(a). Instead of painting the scintillator sheets black, which was previously chosen to provide both optical isolation and reduce internal reflection for the highly-sensitive CMOS sensor, sheets of aluminized Mylar foil 6 μm thick cut to the same size as the scintillator were used between each scintillator sheet. This increases the internal reflection of the scintillator while providing optical isolation that does not permanently modify the scintillator. Further motivation for this design choice and results of the efficiency of the optical isolation are discussed in section 5.1. The scintillator stack is assembled by placing scintillator and Mylar sheets one-by-one into the stack holder. When fully assembled, the total detector thickness is 39.9 mm, giving an average sheet thickness (including Mylar foil) of 2.85 mm. The assembled detector prototype is shown in figure 2(a).

To package the detector and electronics into a single unit, a 3D-printed enclosure was designed into which the scintillator stack was placed, with external mounts for the electronics (described in the next section) and PC. The CAD schematic for the detector enclosure is shown in figure 1(b) with photos shown in figures 2(b)–(d). The enclosure features two mounts at the front and back of the detector to allow for the entire enclosure to be mounted onto the beam nozzle in either direction. The beam nozzle at the CCC, shown in figure 2(e), is a brass tube 70 mm in length and diameter, which has a pin 10 mm in length and 3.0 mm in diameter that protrudes 4.0 mm from the end of the nozzle. The detector nozzle mount has a slot for the pin that allows the detector to be mounted at a 90 degree angle and then rotated such that the nozzle pin stops rotation once the detector is upright

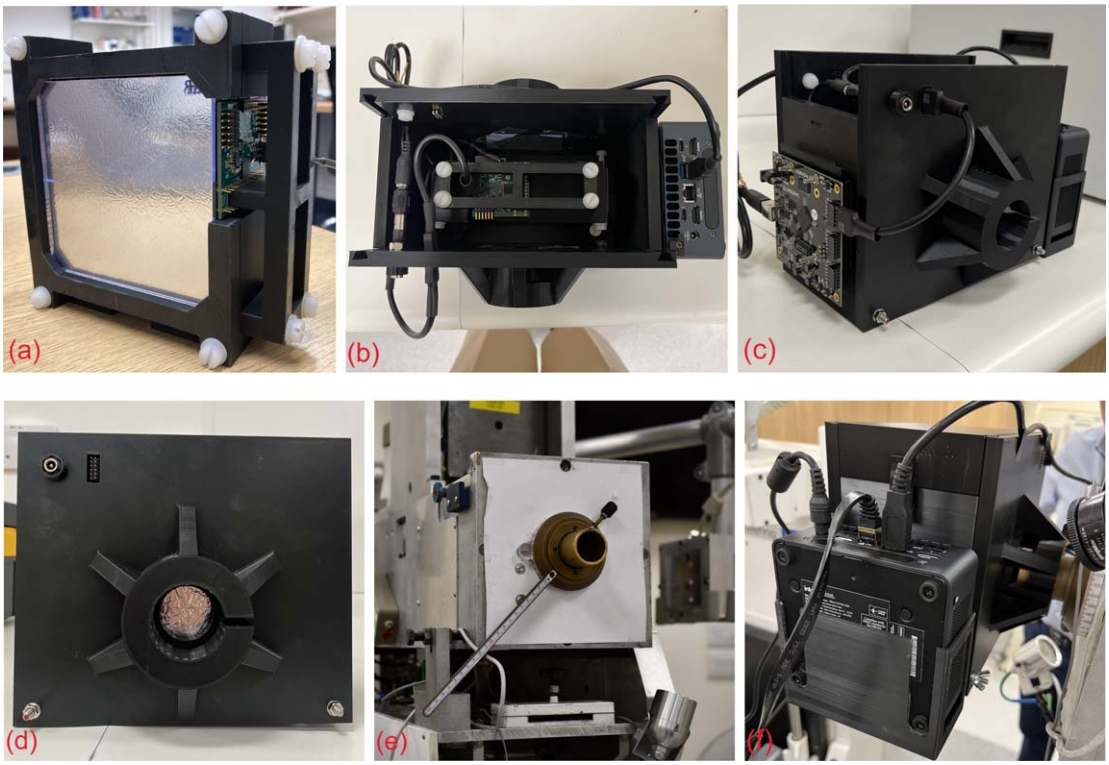

Figure 2. Prototype module for the CCC experiment showing several views of the scintillator stack, electronics and detector enclosure. (a) 3D-printed scintillator stack enclosure with 14 clear, polished sheets coupled to a DDC232 board. (b) Top view of detector enclosure with lid removed showing scintillator stack placement and DDC232 power and data connections. (c) Detector enclosure side-view showing USB104 A7 FPGA board with USB and Pmod feed-through connections. (d) Beam's eye view of detector enclosure showing nozzle mount and Mylar window. Mount is mirrored on rear face of enclosure. (e) Brass beam nozzle at Clatterbridge. The pin at the top of the nozzle is used to secure the detector enclosure in place. (f) Detector enclosure mounted onto the beam nozzle with a view on the NUC PC and power/data/network connections. The enclosure is mounted at a 90 degree angle and then rotated to secure against the pin on the beam nozzle under the weight of the detector itself.

as shown in figure 2(f). Mounting the detector onto the beam nozzle itself rather than on the treatment couch significantly reduces uncertainty associated with setup misalignment, in particular with ensuring the scintillator sheets are perpendicular to the beam axis. If incorrectly aligned, the range accuracy worsens since the path length of the proton beam in the detector changes with the cosine of the angular rotation. Providing nozzle mounts at both the front and back of the detector allows for range measurements in either direction in the scintillator stack. This helps to mitigate scintillator ageing from radiation damage: if most of the dose is delivered in the back half of the detector (i.e. in the Bragg peak), the detector can be flipped and re-calibrated (see section 4.2.1) to extend the life of the scintillator sheets. Beam transport into the detector enclosure is facilitated via light-tight 6 μm thick aluminized Mylar foil windows at each nozzle mount.

4.1.2. Electronics

The detector uses Hamamatsu S12915-16R photodiodes with an effective photosensitive area of 6.0 mm^2 and spectral response wavelength range of 340–1100 nm (Hamamatsu Photonics 2019). The photodiode quantum efficiency peaks at 960nm but demonstrates good sensitivity across the visible wavelength spectrum. This particular model was chosen for its low cost, physical dimensions and its availability off-the-shelf. A Texas Instruments DDC232-CK ADC is used to perform photodiode current integration. The DDC232 is a low-power 32-channel ADC featuring zero-deadtime dual-integrators with integration times between 166.5 μs-1 s, 20-bit precision and 8 assignable full-scale ranges (FSR) from 12.5 to 350 pC (Texas Instruments 2010). The DDC232 therefore provides large headroom, excellent digitisation precision and is fast enough to keep up with modern spot-scanning systems. As with the photodiodes, this ADC is readily available commercially off-the-shelf. The photodiodes and DDC232 are integrated on a compact custom-made circuit board designed by Cosylab, shown in figures 3(a) and (b), which houses 16 photodiodes spaced 2.86 mm apart, matching the physical size of the photodiodes exactly. The current signal from each photodiode is split across two DDC232 inputs, which essentially doubles the headroom of the ADC and minimises the risk of saturation. As the detector only uses 14 scintillator sheets, the first two photodiode inputs on the circuit board are left empty. The photodiodes are contact coupled directly to the scintillator sheets, as the pressure applied by the circuit board clamping mount

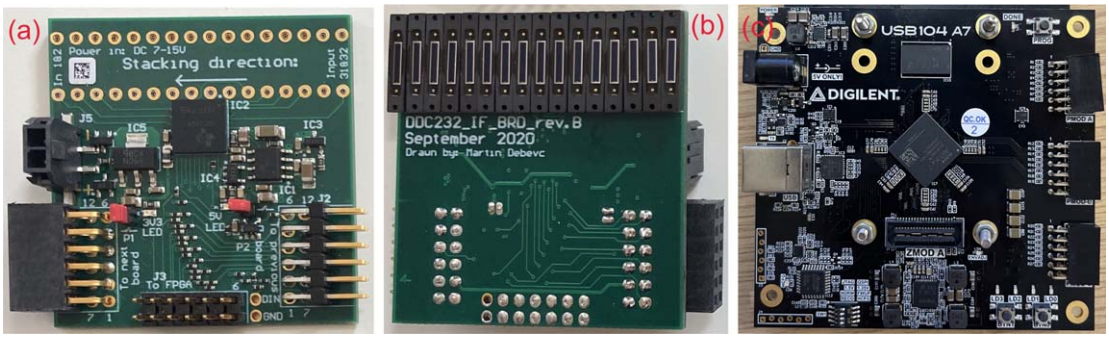

Figure 3. QuARC front-end electronics. (a) Front view of custom DDC232 circuit board. The Pmod junctions on the left and right of the board facilitate daisy-chaining while the central junction connects to the FPGA. (b) Back view of custom DDC232 circuit board showing the Hamamatsu S12915 photodiodes. (c) Digilent USB104 A7 FPGA development board. The custom DDC232 circuit is connected to one of the three available Pmod junctions on the board.

behind the photodiodes enabled sufficient light collection without the need for optical gel. With the photodiode spacing on the circuit board exactly matching the scintillator sheet thickness, alignment of the photodiodes with the corresponding scintillator sheet is achieved by aligning the leading edge of the circuit board with the front of the scintillator face. The DDC232 chips can also be daisy-chained to increase the number of available channels and the custom circuit boards facilitate this via connections at each end of the board. This modular design capability however is not required in this work and will instead be explored in future studies.

The DDC232 circuit boards are read-out by a Digilent USB104 A7 FPGA development board, shown in figure 3(c) (Digilent 2023). Connection to a PC is made via USB 2.0, which also provides 5V power for the USB104. For the DDC232 circuit board, data connection to the FPGA is made via a peripheral module (Pmod) interface using a 10-pin jumper cable, with 12 V power being provided separately, as shown in figures 2(b) and (c). Data acquisition (DAQ) is performed using a compact Intel NUC PC (Intel 2023), with the user-specified number of digitised photodiode charge results acquired at a rate of up to 6 kHz. The software back-end also provides a live display of the photodiode charge levels at 50 Hz as well as live function-fitting for real-time range reconstruction at up to 5 Hz.

4.2. Data analysis

4.2.1. Calibration

To calibrate the detector for a proton range measurement, background and so-called 'shoot-through' measurements are first required. The specific methodology for how these calibration measurements were acquired is discussed in section 5.2, however an overview of the principles is provided here. The background measurement is taken at the start of each experiment with the beam switched off. The resulting background, typically less than 1% of the amplitude of a measured signal, is then subtracted from the raw photodiode charge levels. The shoot-through measurements are used to calibrate the detector for differences in individual scintillator sheet light output, photodiode response and photodiode-sheet coupling by making use of the plateau region in the Bragg curve of a 245 MeV proton beam, the highest energy typically available at a standard proton treatment centre. By shooting a high-energy proton beam through the centre of the front and back of the detector module and then averaging and normalising to take into account the slight tilt in the curve plateau, a relatively flat light response in the detector can be achieved. This is possible due to the minimal scintillator light quenching in this region of the Bragg curve. A small amount of absorber is placed in front of the detector during this measurement (typically around 5 cm) to account for the small dose build-up at the start of the Bragg curve (Kelleter *et al* 2019). This calibration provides a multiplicative calibration factor for each photodiode in the setup.

To produce a fitted curve, the acquired photodiode exposures (typically around 30000, corresponding to 5 s of exposure) are averaged, calibrated and histogrammed with the depth axis converted to water-equivalent thickness (WET). Depth calibration uses the physical thicknesses of the individual scintillator sheets and Mylar foil, and the measured relative stopping power to water (RSP) of the stack. While the shape of the Bragg curve is relatively easily recovered, accurate depth calibration is crucial in order to achieve sub-mm range reconstruction accuracy. The WET of each sheet can be found using equation (1). Measurement of the single RSP factor is discussed in section 5.2.

$$\text{Sheet WET} = \text{Physical Thickness (Sheet} + \text{Foil)} \times \text{RSP}. \quad (1)$$

4.2.2. Function fitting

To recover the proton range, the depth-light data is fitted with a numerical model developed by Laurent Kelleter in Kelleter and Jolly (2020), where the range was found to be accurate to within 0.2 mm compared to Monte Carlo simulation. As mentioned previously, scintillation light output becomes non-linear with energy deposition in regions of high LET (around the Bragg peak) and this effect must be taken into account for range reconstruction. This so-called 'quenched Bragg (QB) model' takes Thomas Bortfeld's mathematical approximation of the proton Bragg curve (Bortfeld 1998) and applies Birks' law for scintillation light quenching (Birks 1951), such that a depth-light curve can be fitted using only a few free parameters, one of which being the proton range. A major advantage of this model is that the proton depth-light curve can be fitted without separate modelling of the LET distribution, which must be simulated and is susceptible to misalignment errors (Wang *et al* 2012). The final mathematical expression for light output, $Q(z)$, using the Kelleter model is given in equation (2).

$$Q(z) = \int_0^{R_0} \frac{1}{\rho}\left[\Phi_0 \frac{1+\beta(R_0-z')}{1+\beta R_0} \frac{S}{\left(\frac{1}{p\alpha^{1/p}}(R_0-z')^{1/p-1}\right)^{-1}+kB} + \gamma\Phi_0\frac{\beta}{1+\beta R_0} \times \int_{z'}^{R_0} \frac{S}{\left(\frac{1}{p\alpha^{1/p}}(R_0-z'')^{1/p-1}\right)^{-1}+kB} dz''\right] \frac{1}{\sqrt{2\pi}\,\sigma_R} \exp\left(-(z-z')^2/2\sigma_R^2\right) dz' \tag{2}$$

The free and fixed parameters used in the Kelleter model are summarised in table 1. Birks' constant, kB, which is a material property that quantifies the amount of quenching, has not yet been experimentally measured for the scintillator used in this work and is therefore left as a free fit parameter. The Kelleter model is implemented using the data analysis framework `ROOT` (Brun and Rademakers 1997), where the model is fitted to the integral of each scintillator sheet bin to partially compensate for the coarse spatial resolution of the detector. Setting $S = 1$ and $kB = 0$ recovers Bortfeld's description of the Bragg curve, allowing for the non-quenched Bragg curve to be reconstructed from the fit result. The resulting Bragg depth-dose curve is then compared against facility reference depth-dose data (typically measured using a water tank and ionisation chamber setup) to determine the accuracy of the range reconstruction and Bragg curve shape.

A new application of the Kelleter model has been implemented as part of this work to enable measurements of spread-out Bragg peaks (SOBPs) with the QuARC. This framework makes an analogous extension to the Kelleter model as Jette and Chen did with Bortfeld's model (Jette and Chen 2011), introducing 3 new parameters: the number of Bragg curves, n, the ratio of the plateau width to range, χ, and a flattening parameter for the plateau, p^*. n is fixed to a value dependent on the beam delivery system. In this case, the data acquisition duration is extended to encompass delivery of the entire SOBP and is averaged as with a pristine Bragg peak. The quenched SOBP is given by a weighted sum of individual quenched Bragg curves (equation (2)), each with different ranges. Rewriting Jette and Chen's formulae, the normalised weights, w_k, of the n individual pristine Bragg curves are given by equation (3) with the range, r_k, of each pristine Bragg curve found using equation (4). As before, setting $S = 1$ and $kB = 0$ allows the original SOBP depth-dose curve to be reconstructed using the same weights/ranges found in the quenched SOBP depth-light fit.

$$w_k = \begin{cases} 1-\left(1-\frac{1}{2n}\right)^{1-\frac{1}{p^*}} & \text{for } k = 0 \\ \left[1-\frac{1}{n}\left(k-\frac{1}{2}\right)\right]^{1-\frac{1}{p^*}} - \left[1-\frac{1}{n}\left(k+\frac{1}{2}\right)\right]^{1-\frac{1}{p^*}} & \text{for } k = 1,\ldots,n-1 \\ \left(\frac{1}{2n}\right)^{1-\frac{1}{p^*}} & \text{for } k = n \end{cases} \tag{3}$$

$$r_k = \left[1-\left(1-\frac{k}{n}\right)\chi\right]R_0. \tag{4}$$

5. Detector characterisation

Experiments with the detector prototype were conducted at the CCC, to investigate the range reconstruction accuracy, in particular for short beam ranges where only a few scintillator sheets register a signal, along with the first measurements of SOBPs. The 14-sheet scintillator stack was placed in the 3D-printed detector enclosure,

Table 1. Free parameters in the Kelleter curve fit. Final 3 parameters only used in SOBP fits. Adapted from Kelleter *et al* 2020. © 2020 Institute of Physics and Engineering in Medicine. CC BY CC BY 3.0.

Variable	Description	Value	Unit
ρ	Density of water	1	g cm^{-3}
p	Range-energy relation exponent	1.742	mm/MeV^{-p}
α	Proportionality factor	0.025	1
β	Fluence reduction slope	0.0012	mm^{-1}
γ	Locally absorbed energy fraction	0.6	1
S	Scintillation light constant	10 000	photons/MeV
R_0	Proton range (80%)	Free	mm
Φ_0	Fluence factor	Free	particles mm^{-2}
σ_R	Gaussian range straggling width	Free	mm
kB	Birks' constant	Free	mm MeV^{-1}
n	Number of pristine Bragg curves	Fixed	1
p^*	SOBP flattening	Free	Dimensionless
χ	SOBP plateau to range fraction	Free	Dimensionless

which was mounted onto the proton beam nozzle as shown in figure 2(f), emulating a realistic mechanical setup for daily clinical use. For all measurements, a DDC232 integration time of 170 μs and FSR of 12.5 pC was used. Each run typically recorded 30 000 photodiode measurements, corresponding to around 5 s of exposure. Experiments were also conducted at University College London (UCL) to determine the efficacy of the Mylar foil optical isolation and to acquire necessary calibration measurements.

5.1. Cross-talk measurements

Past experience with a highly-sensitive CMOS sensor required scintillator sheets to be painted black to reduce the internal reflection and light output of the scintillator (Kelleter *et al* 2020). However, with the large dynamic range of the new photodiode-based system, the opposite was required, thus motivating a new method for optical isolation. An attempt was first made to strip the previously black-painted sheets and repaint them white, however this process was found to permanently damage the scintillator. Typical methods used in high-energy physics to both optically isolate scintillator and increase internal reflection involve wrapping the scintillator with aluminized Mylar foil (Arnold *et al* 2005), chosen for its high reflectivity and minimal impact on particle transport. However, with the segmented detector design, wrapping each sheet individually and uniformly, leaving one edge exposed for light collection, and then assembling into a stack would be far too impractical. Instead, a compromise was found by utilising sheets of opaque aluminized Mylar foil 6 μm thick, cut to the same size as the scintillator sheets, placed between each scintillator sheet to provide optical isolation.

An experiment was conducted in an electronics lab at UCL using an LED fibre to inject blue light into the scintillator through a small hole drilled into the sheet (facing opposite to the photodiodes), with the goal to measure the cross-talk in neighbouring sheets and determine the effectiveness of the optical isolation of the Mylar foil. LED fibres were injected into two sheets with one unilluminated sheet placed in-between and either side of the lit sheets. This allowed for the cross-talk to be measured in cases with one and two neighbouring sheets contributing light spill into dark sheets. Figure 4 shows results for the following cases: (a) no optical isolation between sheets and Mylar foil optical isolation with the stack assembled in (b) white and (c) black plastic holders. It was found that using a black stack holder instead of a white holder was necessary to reduce reflection of light leakage from exposed scintillator edges not covered by photodiodes. In this case, cross-talk levels were found to be less than 1%.

5.2. Calibration

As shown in equation (1), the RSP of the scintillator stack material is required to calibrate the depth axis to WET. To find the RSP, a range pullback test was performed in a treatment room at the PBT facility at University College London Hospital (UCLH). The scintillator stack shown in figure 2(a) was placed in a plastic PELI 1510 case (PELI Products S.L.U. 2023), which was aligned to approximately beam iso-centre on the treatment couch. Sections of the small faces of the PELI case were removed and replaced with aluminized Mylar beam entrance and exit windows to ensure minimal scattering and energy loss of the proton beam whilst ensuring that the case remained light tight. The range of a 210 MeV proton beam was measured using an IBA Giraffe with and without the scintillator stack in the upstream PELI case. The difference in the two ranges provides the WET of the scintillator stack and the RSP can be found by dividing this by the physical thickness of the stack. To compensate

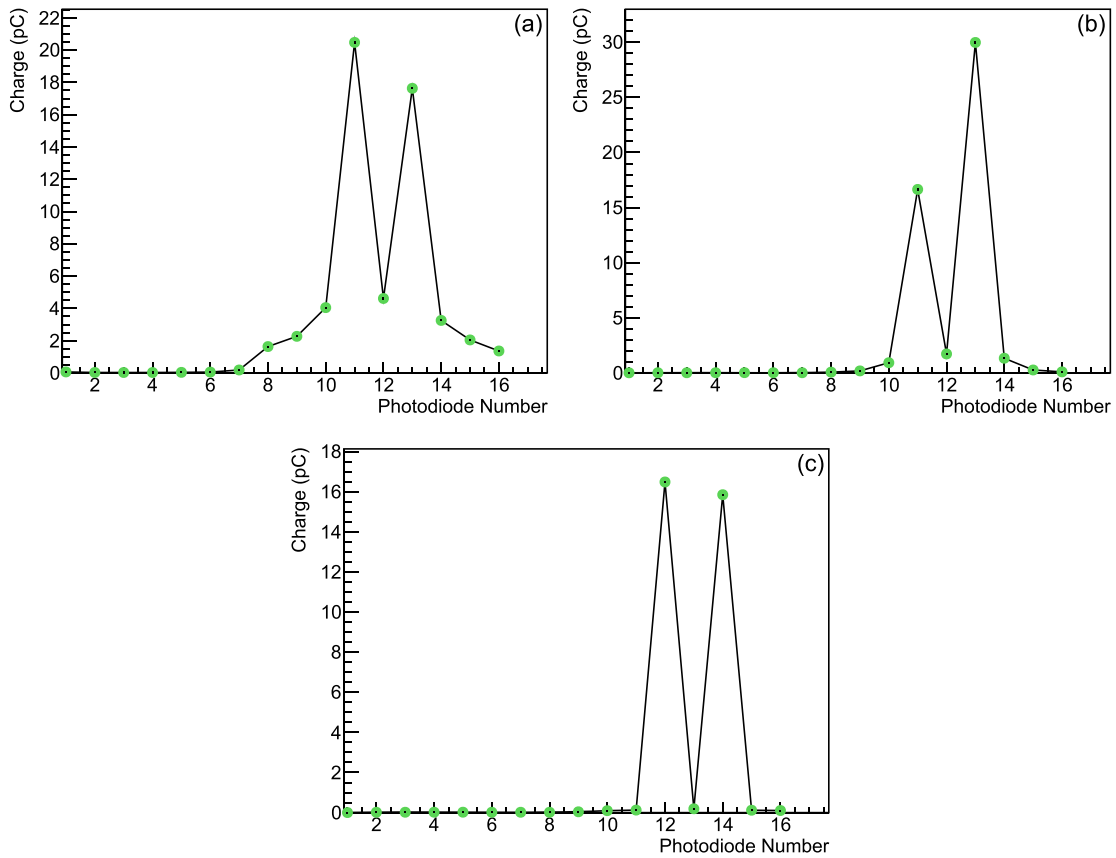

Figure 4. Cross-talk levels when illuminating two sheets (with one unilluminated sheet in between) using an LED fibre, investigating the use of Mylar foil for optical isolation, in differently coloured scintillator stack holders. (a) No optical isolation, white stack holder. This highlights the need for some form of optical isolation when using clear scintillator sheets. (b) Mylar foil, white stack holder. This shows significant improvement, but a non-negligible amount of light leakage remains. (c) Mylar foil, black stack holder. The black holder reduces cross-talk to less than 1%. Note that the stack was disassembled between each test, so the photodiode coupling is not constant.

for the relatively coarse range uncertainty of the Giraffe (0.5 mm), a stack of 25 scintillator sheets (with Mylar foil) of the same type as those used in the detector prototype was assembled for this measurement. The physical thickness of the stack was 71.0 mm and the difference in proton range was found to be 73.4 $\pm$ 0.5 mm, thus giving an RSP of 1.034 $\pm$ 0.007. For simplicity and given the similarity between the energy-dependent stopping powers of water and polystyrene (Berger *et al* 2017), the RSP is assumed to be constant with proton energy.

A background measurement was performed at the CCC where an average charge of 0.013 pC was recorded across the photodiodes. The shoot-through calibration measurements were also performed at UCLH during the same test as the WET measurements described above, given the limited proton beam energy available at the CCC. This measurement used a 245 MeV beam with ion-source current 18.8 nA and approx. spot size 7 mm FWHM through the centre of the front and back of the scintillator stack, with 57 mm of solid water placed upstream of the detector. The front and back shoot-through measurements can be seen in figure 5(a). A clear difference is observed in the slope of the two curves, which demonstrates the necessity of normalising and averaging the two to achieve a flat depth-light distribution, which is shown in figure 5(b). Less than 10% variation sheet-to-sheet in the overall light output is observed.

To provide qualitative information about the calibration stability, a 70 MeV proton beam was measured after calibration at UCLH for comparison against pencil-beam measurements at the CCC. The raw and calibrated curves for the 70 MeV beam at UCLH (11 mm FWHM) and 60 MeV beam at the CCC (34 mm FWHM), both through the centre of the scintillator stack, are shown in figure 6. A simple visual inspection shows discontinuities on the order of 10% in the Clatterbridge depth-light curve (PDL) when compared to the PDL measured at UCLH, suggesting the coupling between the photodiodes and scintillator had changed slightly between the experiments (8 months apart). The calibration measurements should in principle remain valid across facilities provided the detector is not disassembled and the beam spot position is the same. While this was the case, the scintillator stack was repeatedly handled between the two experiments during prototyping of the 3D-printed detector enclosure, which may have shifted the DDC232 circuit board and therefore caused the

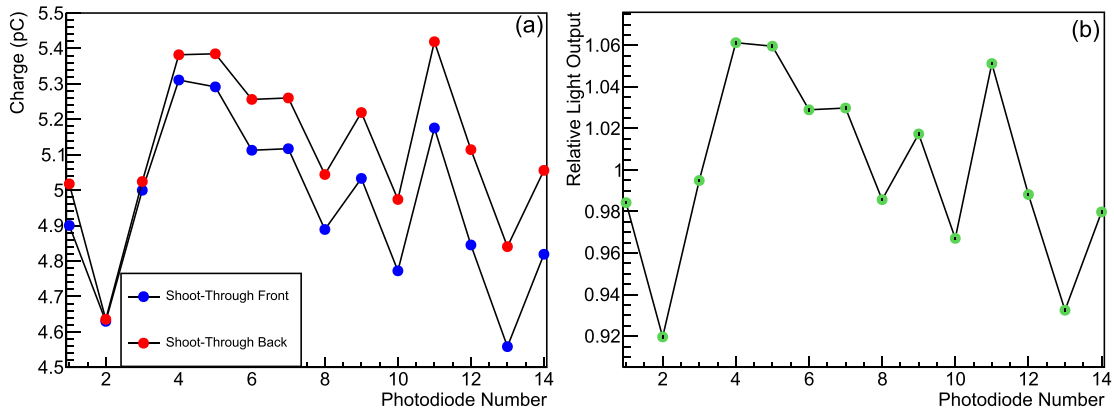

Figure 5. (a) Front and back calibration shoot-through measurements and (b) resulting normalised and averaged calibration curve.

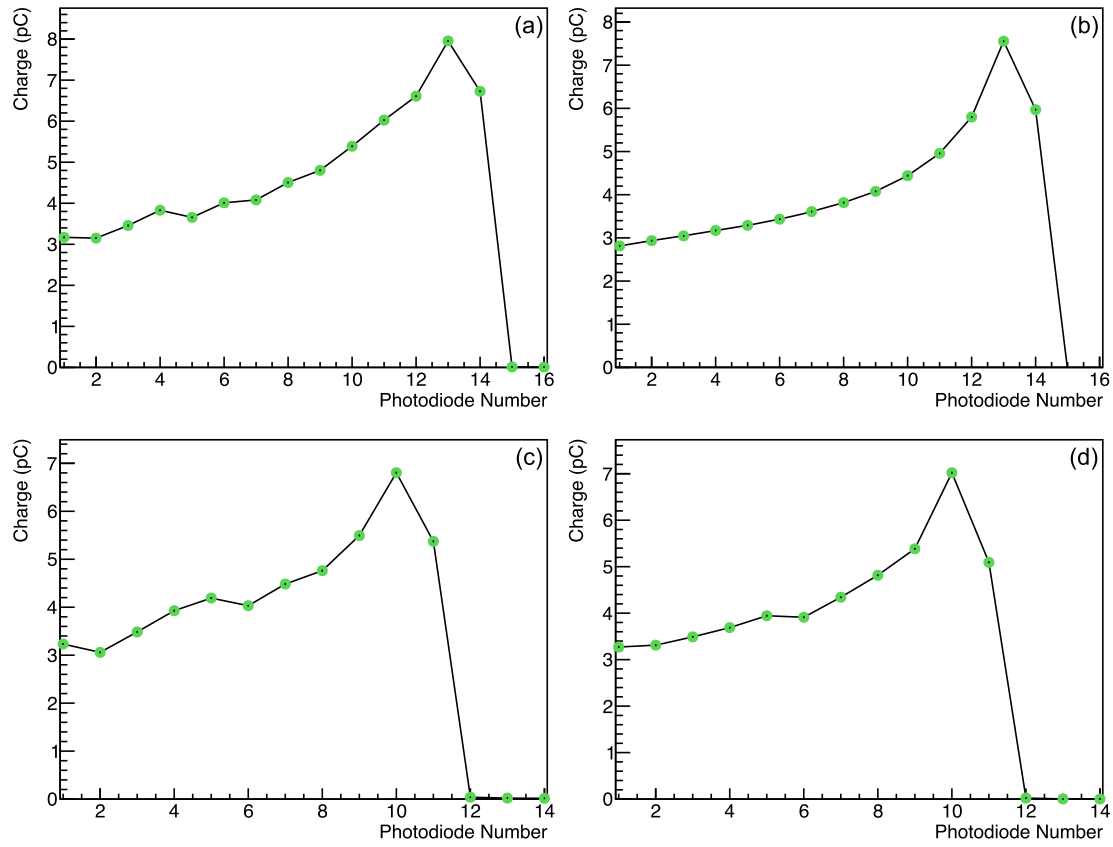

Figure 6. Raw (a) and calibrated (b) 70 MeV curve measured at UCLH and raw (c) and calibrated (d) 60 MeV curve measured at the CCC.

photodiode-scintillator coupling to change. Addressing this effect in the long-term is discussed in section 6.5 with an interim solution provided in the next section.

5.3. Pencil beam measurements

To determine the range accuracy of the QuARC, range measurements of the 60 MeV pristine proton beam Bragg curve were performed at the CCC with increasing amounts of PMMA absorber: 0–10 mm in 1 mm steps and 10–20 mm in 2 mm steps. Note that these thicknesses are quoted in terms of eye-tissue equivalent (ETE), which is the standard used at the CCC, where 1 mm ETE corresponds to 1.05 mm WET. This tested the range reconstruction ability with exceedingly few data points (only 5 sheets with 20 mm ETE of absorber) and its sensitivity to 1 mm ETE changes in absorber thickness. Figure 7 shows fit results for absorber thicknesses of

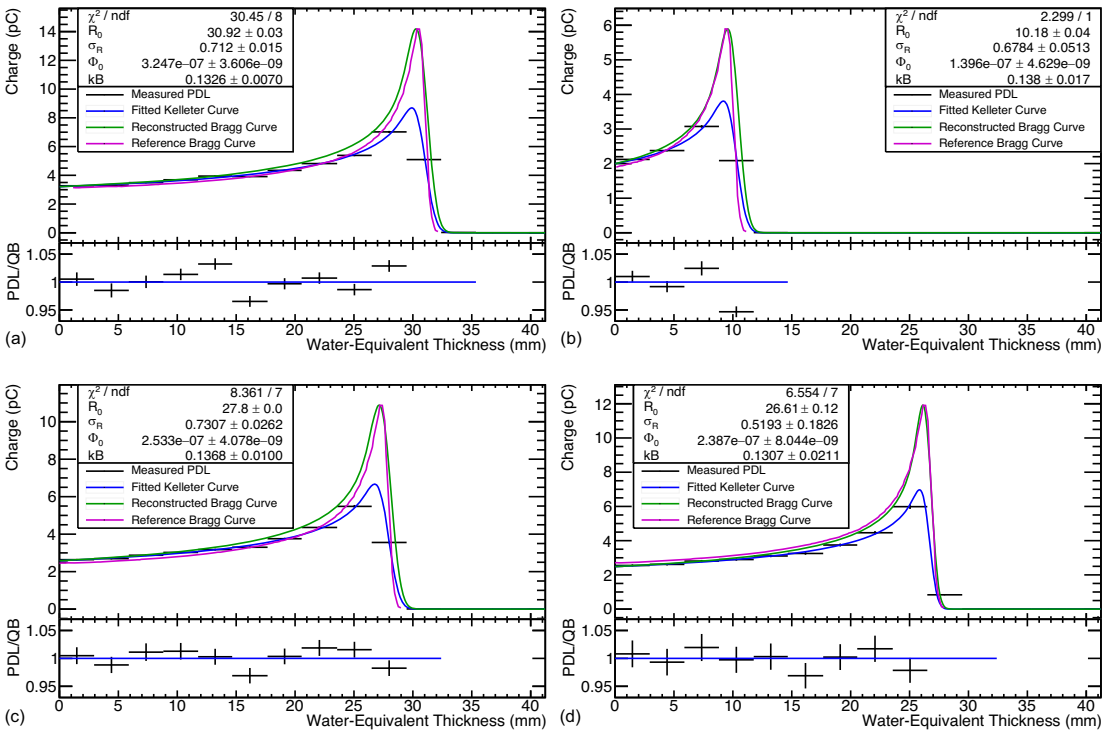

Figure 7. Fit results for the 60 MeV proton beam (1 nA nozzle current) with: (a) 0 mm, (b) 20 mm, (c) 3 mm and (d) 4 mm ETE absorber thickness. The width of the black horizontal bars represents the WET of each scintillator sheet. The blue curve is the fitted quenched Bragg curve and the green curve is the reconstructed Bragg curve (i.e. $kB = 0$). Only the fit uncertainty is shown in R_0. The reconstructed Bragg curve is normalised to be equal to the quenched Bragg curve at 0 mm. The magenta curve shows the facility reference depth-dose curve and is normalised to match the height of the reconstructed Bragg curve. The reference ranges are: (a) 30.85 mm (b) 9.85 mm (c) 27.70 mm (d) 26.65 mm, all with uncertainty ±0.10 mm. The residual plot shows the ratio between the measured depth-light curve and the Kelleter curve.

0 mm, 3 mm, 4 mm and 20 mm ETE, where an RSP of 1.034 was used to calibrate the depth axis. A reference depth-dose curve for the 60 MeV beam was provided by the facility, which is then shifted in the depth axis by the known absorber WET for comparison against the reconstructed Bragg curve. To compensate for the sub-optimal light output calibration, the sheet light output uncertainty was increased by a factor of 10, which was estimated from the standard deviation of the agreement between the measured light output and the Kelleter curve, but maintains relative differences in the uncertainty across photodiodes and measurement runs. Range uncertainty calculation is discussed further in section 6.1.

The range reconstruction is consistently accurate to within 0.2 mm when compared to the reference for up to 18 mm ETE absorber thickness. There is however significant variation in the width of the reconstructed Bragg curve (σ_R) peaks. This is most apparent in the cases with 3 mm and 4 mm absorber (figures 7(c) and (d) respectively), which shows the difference in the reconstructed Bragg curve shape depending on the placement of the Bragg peak either entirely within a sheet or between two sheets. The reconstructed Bragg curve has an inflated σ_R when the Bragg peak is mostly placed in between two scintillator sheets, an effect which is exacerbated by the small number of data points and the sharp peak of the 60 MeV beam.

To investigate the influence of the curve shape on the range reconstruction accuracy, a comparison was made between the range reconstruction with free parameters and with Birks' constant and sigma fixed. This would help determine whether it is beneficial to fix these parameters in cases where they are known accurately, in particular as Birks' constant is in principle a material property. As Birks' constant was found to be relatively stable in the fit results, an average value of 0.13 MeV mm^{-1} was used and a suitable value for σ_R of 0.55 mm was chosen, slightly larger to that in figure 7(d). The accuracy of the reconstructed range for free and fixed Birks' constant and sigma is shown in figure 8 where it can be seen that the fixed parameter fits reconstruct the range slightly more accurately, generally correct to 0.1 mm for up to 18 mm ETE absorber. In both cases, 18 mm and 20 mm ETE absorber case are exceptions, where the accuracy worsens due to there being fewer than 5 data points in the fit. Given a minimum range uncertainty of 0.1 mm in both the reference and reconstructed ranges, this improvement to the range accuracy may not be significant and fixing sigma is generally not practical, as this parameter changes with beam energy and is used to detect changes in the beam energy spread. Nevertheless, these results show that not only does the range reconstruction work at very shallow depths with few data points,

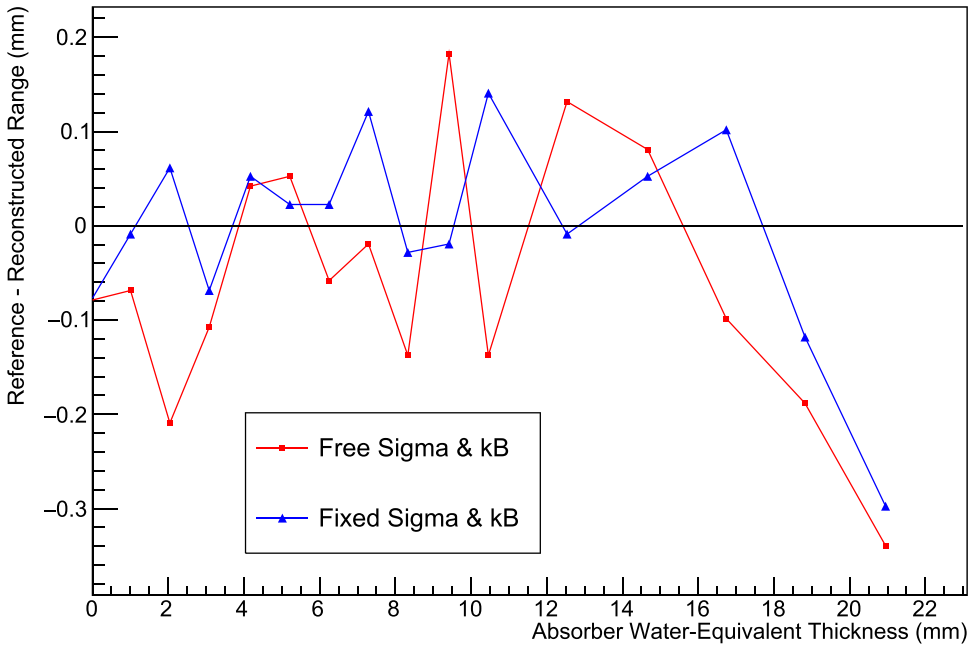

Figure 8. Range reconstruction accuracy for a 60 MeV beam with increasing amounts of absorber, for free and fixed values of sigma and Birks' constant. For the fixed parameter fits, $\sigma_R = 0.55$ mm and $kB = 0.13$ MeV mm^{-1} was used. A range accuracy of ± 0.2 mm is considered to be clinically acceptable.

but that the detector is sensitive to 1 mm shifts in range and even with sub-optimal light output calibration, the range can be reconstructed accurately to within 0.2 mm.

5.4. Spread-out Bragg peak measurements

To investigate the ability of the detector to measure and perform a fit to a SOBP, three different SOBPs were chosen, providing a range of typical treatment plans used in the CCC. The range modulator wheel rotates at approximately 400 rpm: since each wheel has 4 symmetrical arms (delivering 4 SOBPs per revolution), this results in the delivery of a full SOBP in ~40 ms. With an integration time shorter than 200 μs, the DDC232 can measure the individual Bragg curves that make up each SOBP, with the resulting delivered SOBP displayed in real time. The characteristics of the chosen SOBPs for the experiment are summarised in table 2.

To fit a quenched SOBP, two additional free parameters are introduced into the fit: χ, the ratio of the range and the modulation of the SOBP and p^*, which is the exponent of the Bragg–Kleeman rule (Bragg and Kleeman 1905), but allowed to vary in order to remove the tilt in the plateau of the reconstructed SOBP (Jette and Chen 2011). While technically the same parameter, p^* is independent to p, which is used in equation (2). A final fixed parameter, n, which is the number of constituent pristine Bragg curves used to make the SOBP, is also introduced and is equal to the number of steps in the range modulator wheel. For each SOBP measurement, 100 000 photodiode measurements were taken using an integration time of 170μs, corresponding to around 15 s of exposure. Fit results using an RSP of 1.034 for the SOBPs listed in table 2 are shown in figures 9(a), (c) and (e).

In each case, the fitted range of the SOBP was accurate to within 0.3 mm of the nominal reference range and with similar residuals between the quenched SOBP and measured light output when compared to pristine Bragg curve fits. In addition, χ was recovered correct to within 8% in all cases, though it should be noted that an upper limit for χ of 1 was put into place, as this parameter cannot physically be larger than 1. The difference can at least be partially attributed to a slight difference between the model and facility definition of the SOBP modulation: the model uses the difference between the ranges of the proximal and distal pristine Bragg curves used to create the SOBP whereas the CCC definition uses the difference between the distal and proximal 90% dose points of the SOBP itself. The most apparent issue with the fits in general is the persisting tilt in the reconstructed SOBP when compared to the reference, which is correlated to an underestimated value of p^*.

It is believed that this systematic underestimation of p^* is due to the shape of the measured depth-light curve: the downward slope in the depth-light curve is caused by the fact that there is more light quenching in the distal region of the SOBP plateau than in the proximal region. In the former, the dose contribution is primarily from the Bragg peak of the highest energy Bragg curve whereas in the latter, the dose contributions are from many superimposed Bragg curve plateaus which therefore experiences less light quenching. While this is an effect that did not need to be considered when the scheme laid out by Jette and Chen was developed, arbitrarily varying p^*

Table 2. SOBP properties. The range is equal to the nominal range of the pristine 60 MeV Bragg peak (30.8 mm) minus the absorber thickness. The modulation is equal to the difference between depth of the proximal and distal 90% dose points. Note that the CCC quotes ranges at 90% of the peak dose, rather than at 80% as used in this work, which was found to be 0.1 mm larger than the quoted 90% range. All lengths given in WET.

Modulator Ref. No.	292/92	172/91	769/02
Absorber (mm)	0.6	5.7	0
Range (90%) (mm)	30.2	25.1	30.8
Modulation (mm)	14.8	17.3	30.8
χ = Modulation/range	0.49	0.69	1
n = Range steps	16	19	33

was still found to be necessary to recover a suitable plateau tilt even with depth-dose curves (Jette and Chen 2011). It was found that fixing p^* to a value of 1.75 (around 10% increase) produced consistently accurate slopes in the reconstructed SOBPs and the results can be seen in figures 9(b), (d) and (f).

With p^* fixed to 1.75, the tilt of the reconstructed SOBP plateau is corrected and the reconstructed range is now accurate to within 0.2 mm. There remains a generally wide spread in the fitted value of Birks' constant across both the different fitted SOBPs and when comparing the cases where p^* is fixed versus a free parameter. The most prevalent issue remaining in the reconstructed SOBPs is the underestimation of the dose in the distal region of the SOBP drop-off. It is believed that this is also due to the different amounts of quenching in the SOBP plateau, where the increased quenching in this distal region skews the fit to underestimate the sharpness of the drop-off. It is possible that this effect is made worse by the relatively poor spatial resolution at such shallow depths, though it does not appear to have a significant impact on the range reconstruction accuracy. This underestimation of the distal drop-off dose means that the weight of the most distal Bragg curve is lower than expected and results in a subtlety in the reconstructed SOBP: the fitted range, which corresponds to the range of the most distal Bragg peak in the SOBP, is greater than the reference range, despite the apparent visual underestimation of the distal drop-off dose.

6. Discussion

6.1. Range uncertainty

Compared to the previous version of the QuARC (Kelleter *et al* 2020), a simpler approach has been adopted in this work to calculate the range uncertainty for the detector. The uncertainty on the raw light output of a scintillator sheet has two main contributions that are added in quadrature: the integral linearity of the DDC232 ADC, which is quoted as $\pm 0.05\%$ of the measured value (Texas Instruments 2010), and the statistical uncertainty, which is calculated as the standard deviation divided by the square root of the total number of measurements (Hughes and Hase 2010). These are then propagated in quadrature when calibrating the light output with shoot-through corrections and background subtraction. With a typical measurement run of 5 s (30 000 photodiode exposures), this scintillator sheet light output uncertainty is generally no more than 0.1%. To better take into account systematic effects from the calibration process, which as discussed in section 5.2 was sub-optimal, the uncertainty was increased by a factor 10, estimated using the deviation from the Kelleter model fit. The systematic uncertainty for the Kelleter model itself was previously found to be ± 0.2 mm (Kelleter and Jolly 2020), which takes into account the accuracy of the empirical Birks' Law estimation, the fit range and the use of Birks' constant as a free fit parameter.

The largest source of uncertainty remaining is the uncertainty in the WET of the plastic scintillator sheets, which is used to calibrate the depth axis as shown in equation (1). The primary contribution to this uncertainty, which increases with proton range, is the uncertainty on the RSP measurement of the entire stack, which was measured to be 1.034 ± 0.007. As the detector was mounted onto the beam nozzle itself, uncertainty on the detector WET due to rotational and translational error is assumed to be negligible. Combining in quadrature the systematic uncertainties of the Kelleter model and WET measurement gives the following range result for the pristine 60 MeV proton beam shown in figure 7(a): $R_0 = 30.9 \pm 0.3$ mm. Both the fitted range result and the uncertainty have been rounded to 0.1 mm, which is typically the precision of interest for clinical range QA measurements. The uncertainty can be reduced to 0.2 mm with more precise measurement of the detector WET, but is estimated to increase to up to 0.5 mm at the highest clinical proton energy of approximately 250 MeV. This range uncertainty however remains comparable to existing commercial devices (Bäumer *et al* 2015).

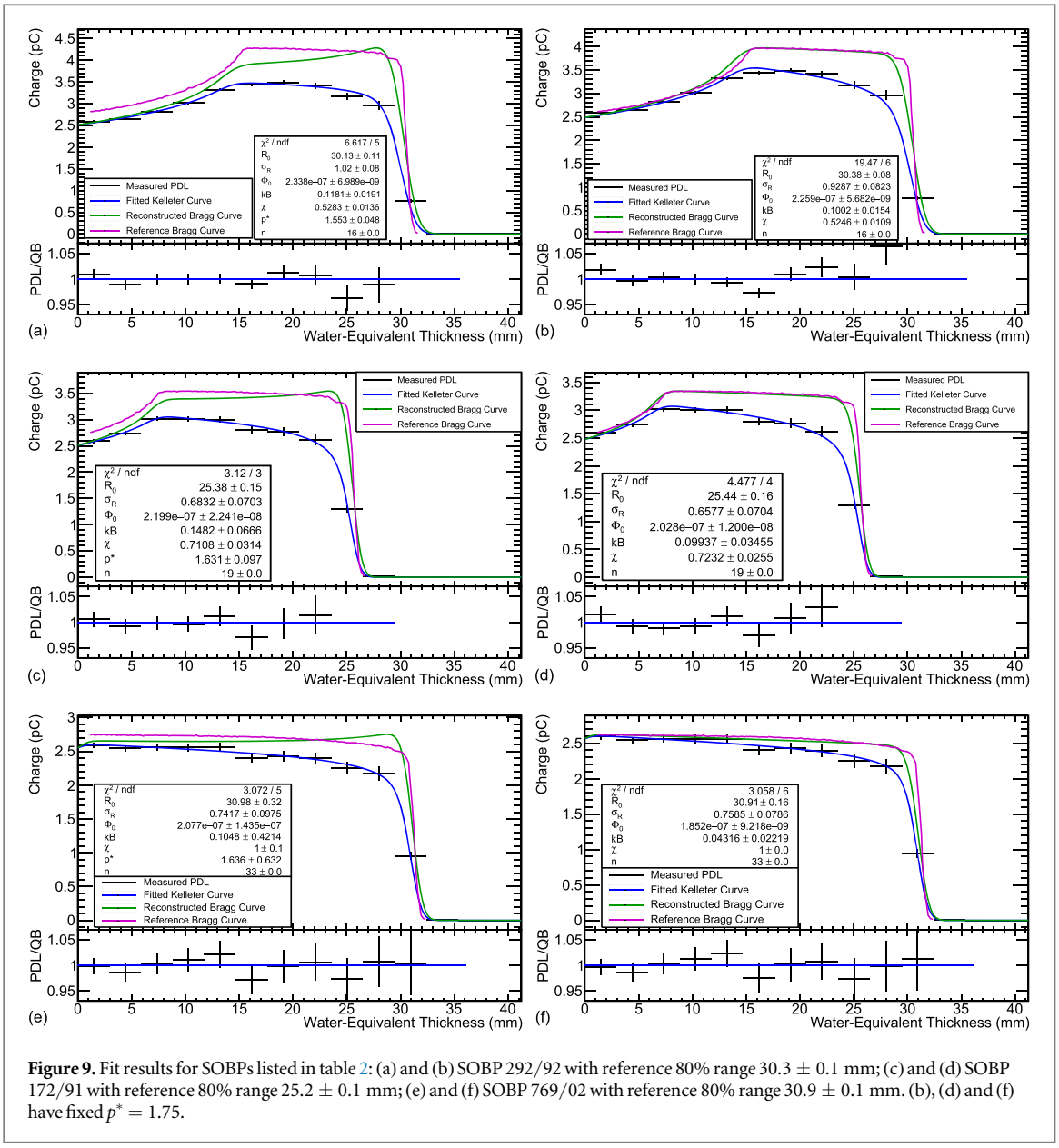

Figure 9. Fit results for SOBPs listed in table 2: (a) and (b) SOBP 292/92 with reference 80% range 30.3 ± 0.1 mm; (c) and (d) SOBP 172/91 with reference 80% range 25.2 ± 0.1 mm; (e) and (f) SOBP 769/02 with reference 80% range 30.9 ± 0.1 mm. (b), (d) and (f) have fixed $p^* = 1.75$.

6.2. Birks' constant

Throughout this work, Birks' constant has been left as a free fit parameter since an accurate value for the detector scintillator has not yet been experimentally measured. In principle, the Kelleter model can be used to determine a value of Birks' constant through fitting an entire depth-light curve, where there is sufficient information about the peak-to-plateau ratio and therefore the amount of quenching observed (Kelleter 2020). Measurements shown in figures 7 and 9 return values of *kB* typically between 0.10 and 0.14 MeV mm^{-1}, a similar order of magnitude to results found for polystyrene scintillators in existing literature (Badhwar *et al* 1967, Hirschberg *et al* 1991, Jang *et al* 2010, Wang *et al* 2012, Alsanea *et al* 2018, Christensen *et al* 2019). Birks' constant could be fixed as it is in principle a material parameter, however whether the constant in this particular detector system is independent of factors like beam energy, scintillator age or even temperature has not been investigated. Nevertheless, while the improvement in the range accuracy seen in figure 8 is not necessarily significant in the low-energy regime investigated here, it is possible that fixing Birks' constant could offer more substantial range stability in the higher clinical energy regime. This is also relevant for SOBP fitting as fixing Birks' constant can reduce the larger parameter space from the additional fitting variables. It should be noted however that fixing Birks' constant to an average value of 0.13 MeV mm^{-1} found in figure 7 does not significantly alter the fit results in figure 9, especially the fitted range or the underestimated distal fall-off in the reconstructed SOBP.

6.3. Detector performance

The deployment of the new photodiode-based readout system has significantly increased the detector data acquisition speed and dynamic range. The results show that at clinical current (approx. 1 nA nozzle current), the measured signal peaks at around 8 pC, which is comfortably within the smallest FSR of the detector and only 2% of the total dynamic range. The measured average background of 0.013 pC is therefore less than 0.2% of the peak signal, which combined with the 20-bit resolution ADC presents an excellent signal-to-noise ratio. The 6 kHz data-rate is more than sufficient to keep up with the SOBP delivery system at the CCC, allowing for the range modulation to be seen within individual photodiode exposures, which is made possible by scripts that can replay previously acquired data at a user-assigned speed. It is expected that this will translate to modern pencil-beam scanning systems at general-purpose PBT facilities, allowing for range measurements of individual proton spots within a scanned treatment. Additionally, the custom photodiode circuit boards are substantially easier to handle and can facilitate daisy-chaining to increase the number of scintillator sheets in the detector. Finally, packaging the device in a 3D-printed nozzle-mountable enclosure drastically simplifies detector setup and mitigates setup misalignment uncertainty.

The range accuracy of the detector with both pristine and spread-out Bragg peaks was found to be consistently within 0.2 mm, which agrees within the uncertainty of the detector (0.3 mm) and the reference range measurement (0.1 mm). Moreover, this performance is well-within the requirements of a clinical device and is competitive with current commercial offerings. While the range accuracy is heavily reliant on an accurate RSP measurement of the active detector material (scintillator and Mylar foil) using another system, this measurement should only be required once for the detector's whole operational lifetime. Since the detector has a density close to that of water, the required correction is only around 3% and is less dependent on proton energy than other devices that use non-water-equivalent materials. The use of photodiodes directly coupled to the scintillator allows for direct measurement of scintillator light in a compact volume without the need for any image analysis or optical artefact correction, unlike other camera-based scintillator systems.

6.4. Clinical applications

The QuARC presents a viable alternative to current commercial offerings for daily ocular proton beam range QA. The large headroom available with the DDC232 means that range QA at FLASH dose rates at and above 40 Gy/s should in principle be possible, which will be the subject of a future work. While scintillators have recently demonstrated dose-rate dependence with protons at FLASH dose-rates (Togno *et al* 2022, Kanouta *et al* 2023) on the order of 2% at up to 10^4 Gy/s, further study is required to determine whether this will significantly affect range reconstruction with the QuARC. Investigation into the FLASH performance of the detector is of particular interest given the promising results of hybrid passive-active beam delivery systems that can achieve FLASH dose-rates while maintaining use of the Bragg peak, for which the measurement and fitting of SOBPs would be required (Simeonov *et al* 2022, Zhang *et al* 2022). The CMOS-based detector prototype has shown promise with the monitoring of mixed helium-carbon beams in heavy ion therapy (Volz *et al* 2020), which has now been made more feasible with the real-time beam monitoring capabilities of the new photodiode-based front-end system.

6.5. Further work

Further investigation of the QuARC's performance with pristine and spread-out Bragg peaks at higher energies is necessary to verify the range accuracy across the full clinical energy spectrum. This will involve the development of a new QuARC prototype with multiple modules in series that make use of the DDC232's daisy-chaining capabilities and thus be capable of general-purpose proton range QA. Given the large amounts of headroom available in the ADCs, further work will also investigate the performance of the detector at ultra-high dose rates to demonstrate the QuARCs viability for FLASH PBT QA measurements. As discussed in section 5.2, the calibration was adversely affected by the mechanical stability of the photodiodes. This should not be a concern in future tests as the scintillator stack is now held securely in the detector enclosure and does not need to be handled directly. The mechanical design of the scintillator holder is also being improved to increase the stability of the scintillator sheets and the photodiode circuit mounting. In addition, the Pmod connectors are being replaced with USB-C to minimise disruption to the circuit position. Rather than splitting the photodiode charge, future revisions of the custom DDC232 circuit board will have a 1:1 mapping between photodiodes and DDC232 inputs, providing 32 photodiodes per board and thereby halving the number of boards needed for a full-size clinical prototype.

7. Conclusion

The design and performance of a compact, scintillator-based detector for ocular proton range QA measurements has been presented. The new photodiode-based data-acquisition system increases the detector dynamic range and data-rate by two orders of magnitude, enables a modular detector design, and improves ease-of-use. Development of the software back-end enables real-time monitoring of photodiode light levels and range reconstruction. An experiment conducted at the CCC demonstrated a range accuracy of 0.2 mm with a 60 MeV proton beam using 0–18 mm of absorber, highlighting the sensitivity of the detector to small changes in proton range, however a slight worsening of the accuracy was observed with 20 mm of absorber due to the limited number of data points. An expansion to the Kelleter model for the fitting of proton depth-light curves was implemented to facilitate the measurement of SOBPs using the QuARC, which was successfully deployed. SOBP measurements demonstrated an overall 0.2 mm range accuracy, though a systematic underestimation in the distal dose drop-off was observed, which warrants further investigation at higher energies. This self-contained nozzle-mountable detector package presents a practical solution for the clinic to facilitate real-time, water-equivalent proton range measurements to sub-mm precision.

Acknowledgments

This work was funded by the UK Science and Technology Facilities Council awards ST/R004870/1, ST/V001183/1 and 2320176. The authors have no relevant conflicts of interest to disclose.

Data availability statement

The data that support the findings of this study are openly available at the following URL/DOI: https://www.hep.ucl.ac.uk/pbt/wiki/Proton_Calorimetry/Experimental_Runs/2022/ClatterbridgeQuARC.

Contributors

The manufacture of the custom circuit boards at Cosylab was managed by Marko Levičnik, with circuits drawn by Martin Debevc. The manufacture of the detector scintillator sheets at NUVIATech Instruments was managed by Hana Buresova.

ORCID iDs

Saad Shaikh https://orcid.org/0000-0002-7086-5187
Simon Jolly https://orcid.org/0000-0002-2713-0732

References

Alsanea F *et al* 2018 A real-time method to simultaneously measure linear energy transfer and dose for proton therapy using organic scintillators *Med. Phys.* **45** 1782–9
Arjomandy B *et al* 2019 Aapm task group 224: comprehensive proton therapy machine quality assurance *Med. Phys.* **46** e678–705
Arnold R *et al* 2005 Technical design and performance of the nemo 3 detector *Nucl. Instrum. Methods Phys. Res.*A **536** 79–122
Badhwar G D *et al* 1967 The non-linear response of the plastic scintillator ne102 *Nucl. Instrum. Methods* **57** 116–20
Bäumer C *et al* 2015 Evaluation of detectors for acquisition of pristine depth-dose curves in pencil beam scanning *J. Appl. Clin. Med. Phys.* **16** 151–63
Beaulieu L and Beddar S 2016 Review of plastic and liquid scintillation dosimetry for photon, electron, and proton therapy *Phys. Med. Biol.* **61** R305
Berger M J *et al* 2017 Stopping-power and range tables for electrons, protons, and helium ions *NIST Standard Reference Database 124*
Birks J B 1951 Scintillations from organic crystals—specific fluorescence and relative response to different radiations *Proc. Phys. Soc.* **64** 874
Bonnett D E *et al* 1993 The 62 MeV proton beam for the treatment of ocular melanoma at clatterbridge *Br. J. Radiol.* **66** 907–14
Bortfeld T 1997 An analytical approximation of the bragg curve for therapeutic proton beams *Med. Phys.* **24** 2024–33
Bragg W H and Kleeman R 1905 XXXIX. on the α particles of radium, and their loss of range in passing through various atoms and molecules *London, Edinburgh, Dublin Phil. Mag. J. Sci.* **10** 318–40
Brun R and Rademakers F 1997 Root - an object oriented data analysis framework *Nucl. Instrum. Methods Phys. Res.*A **389** 81–6
Christensen J B *et al* 2019 Ionization quenching in scintillators used for dosimetry of mixed particle fields *Phys. Med. Biol.* **64** 095018
Darne C D *et al* 2017 Performance characterization of a 3D liquid scintillation detector for discrete spot scanning proton beam systems *Phys. Med. Biol.* **62** 5652
Darne C D *et al* 2022 A novel proton-integrating radiography system design using a monolithic scintillator detector: experimental studies *Nucl. Instrum. Methods Phys. Res.*A **1027** 166077

Digilent 2023 USB104 A7 Reference Manual. May 2023 (https://digilent.com/reference/programmable-logic/usb104a7/reference-manual)
Ding X *et al* 2021 A critical review of the practices of proton daily quality assurance programs *Ther. Radiol. Oncol.* **5**
Hamamatsu Photonics 2019 Si Photodiode S12915-16R. Jan. 2019 (https://hamamatsu.com/eu/en/product/optical-sensors/photodiodes/si-photodiodes/S12915-16R.html)
Hirschberg M *et al* 1991 Precise measurement of birks kb parameter in plastic scintillators *Conf. Record of the 1991 IEEE Nuclear Science Symposium and Medical Imaging Conf.* 1 183–6
Hughes I G and Hase T P A 2010 *Random Errors in Measurements. Measurements and their Uncertainties* (Oxford University Press) 1st ednp 14 Ch 2
Intel 2023 Intel NUC 11 Pro Kit NUC11TNKv7 (https://intel.co.uk/content/www/uk/en/products/sku/205607/intel-nuc-11-pro-kit-nuc11tnkv7/specifications.html)
Ion Beam Applications 2023a Giraffe—Single-shot Bragg peak measurement (https://iba-dosimetry.com/product/giraffe)
Ion Beam Applications 2023b Lynx PT—High accuracy and speed for daily machine parameter verification. https://iba-dosimetry.com/product/lynx-pt.
Ion Beam Applications 2023c PPC05 Plane Parallel Ionisation Chamber (https://iba-dosimetry.com/product/ppc05-plane-parallel-chamber)
Ion Beam Applications 2023d Sphinx—Daily QA phantom for PBS pencil beam scanning (https://iba-dosimetry.com/product/sphinx)
Ion Beam Applications 2023e Zebra—Scan monolayer and SOBP measurements (https://iba-dosimetry.com/product/zebra)
Jang K W *et al* 2011 Fabrication and optimization of a fiber-optic radiation sensor for proton beam dosimetry *Nucl. Instrum. Methods Phys. Res., Sect. A* **652** 841–5 Symposium on Radiation Measurements and Applications (SORMA) XII 2010
Jette D and Chen W 2011 Creating a spread-out bragg peak in proton beams *Phys. Med. Biol.* **56** 131
Jolly S *et al* 2020 Technical challenges for flash proton therapy *Phys. Med.* **78** 71–82
Kacperek A 2009 Proton therapy of eye tumours in the uk: a review of treatment at clatterbridge *Appl. Radiat. Isot.* **67** 378–86
Kanouta E *et al* 2023 Time-resolved dose rate measurements in pencil beam scanning proton flash therapy with a fiber-coupled scintillator detector system *Med. Phys.* **50** 2450–62
Kelleter L 2020 A scintillator-based range telescope for particle beam radiotherapy *PhD Thesis* University College London, London, UK (https://discovery.ucl.ac.uk/id/eprint/10119396)
Kelleter L and Jolly S 2020 A mathematical expression for depth-light curves of therapeutic proton beams in a quenching scintillator *Med. Phys.* **47** 2300–8
Kelleter L *et al* 2019 Technical note: Simulation of dose buildup in proton pencil beams *Med. Phys.* **46** 3734–8
Kelleter L *et al* 2020 A scintillator-based range telescope for particle therapy *Phys. Med. Biol.* **65** 165001
Lomax A J 2008a Intensity modulated proton therapy and its sensitivity to treatment uncertainties 2: the potential effects of inter-fraction and inter-field motions *Phys. Med. Biol.* **53** 1043
Lomax A J 2008b Intensity modulated proton therapy and its sensitivity to treatment uncertainties 1: the potential effects of calculational uncertainties *Phys. Med. Biol.* **53** 1027
McManus M *et al* 2020 The challenge of ionisation chamber dosimetry in ultra-short pulsed high dose-rate very high energy electron beams *Sci. Rep.* **10** 9089
NUVIATech Instruments 2019 NuDET PLASTIC Specification Sheet (https://nuviatech-instruments.com/wp-content/uploads/sites/3/2017/12/NVG-375016-Fichesx4-PLASTICAout2019-V3-2.pdf)
Paganetti H 2012 Proton therapy: history and rationale *Proton Therapy Physics* 1st edn (CRC Press) pp 1–19 Ch 1
Particle Therapy Co-operative Group 2023 Facilities in Operation (https://ptcog.site/index.php/facilities-in-operation-public)
PELI Products S.L.U 2023 1510 Protector Carry-On Case Specification Sheet. Aug. 2023 (https://www.peli.com/eu/en/product-pdf/?product=cases&item=32&source=web)
Physikalisch-Technische Werkstaetten 2023 Particle Therapy QA Tools (https://ptwdosimetry.com/en/products/mp3-ppl?downloadfile=951&type=3451&cHash=9f153c45fea1ac05ba289c2fb6c62dcc)
Placidi L *et al* 2018 Range resolution and reproducibility of a dedicated phantom for proton pbs daily quality assurance *Z. Med. Phys.* **28** 310–7
Rana S *et al* 2019 Development and long-term stability of a comprehensive daily qa program for a modern pencil beam scanning (PBS) proton therapy delivery system *J. Appl. Clin. Med. Phys.* **20** 29–44
Robertson D *et al* 2012 Quenching correction for volumetric scintillation dosimetry of proton beams *Phys. Med. Biol.* **58** 261
Robertson D *et al* 2013 Optical artefact characterization and correction in volumetric scintillation dosimetry *Phys. Med. Biol.* **59** 23
Russo S *et al* 2017 Characterization of a commercial scintillation detector for 2D dosimetry in scanned proton and carbon ion beams *Phys. Med.* **34** 48–54
Simeonov Y *et al* 2022 Development, monte carlo simulations and experimental evaluation of a 3d range-modulator for a complex target in scanned proton therapy *Biomed. Phys. Eng. Express* **8** 035006
Su Z *et al* 2020 Evaluations of a flat-panel based compact daily quality assurance device for proton pencil beam scanning (PBS) system *Phys. Med.* **80** 243–50
Texas Instruments 2010 32-Channel, Current-Input Analog-to-Digital Converter Datasheet. Apr. 2010 (https://ti.com/lit/gpn/ddc232)
Togno M *et al* 2022 Ultra-high dose rate dosimetry for pre-clinical experiments with mm-small proton fields *Phys. Med.* **104** 101–11
Ultimaker 2018 Technical Data Sheet Tough PLA. Sept. 2018 (https://cdn.shopify.com/s/files/1/0765/4369/files/UM_TDS_Tough_PLA_RB_V11.pdf?v~=~1584706459)
Volz L *et al* 2020 Experimental exploration of a mixed helium/carbon beam for online treatment monitoring in carbon ion beam therapy *Phys. Med. Biol.* **65** 055002
Wang L L W *et al* 2012 Determination of the quenching correction factors for plastic scintillation detectors in therapeutic high-energy proton beams *Phys. Med. Biol.* **57** 7767
Yap J *et al* 2020 Beam characterisation studies of the 62 MeV proton therapy beamline at the clatterbridge cancer centre *Phys. Med.* **77** 108–20
Zhang G, Gao W and Peng H 2022 Design of static and dynamic ridge filters for flash-impt: a simulation study *Med. Phys.* **49** 5387–99